

## Phase separation in the outer membrane of *Escherichia coli*

Georgina Benn<sup>1,2,3</sup>, Irina V. Mikheyeva<sup>4</sup>, Patrick George Inns<sup>5</sup>, Joel C. Forster<sup>6,7,8</sup>, Nikola Ojkić<sup>6</sup>,  
Christian Bortolini<sup>1</sup>, Maxim G. Ryadnov<sup>3,9</sup>, Colin Kleanthous<sup>5,\*</sup>, Thomas J. Silhavy<sup>4,\*</sup>, Bart W.  
Hoogenboom<sup>1,2,6,7\*</sup>

1. London Centre for Nanotechnology, University College London, London WC1H 0AH, UK
2. Institute of Structural and Molecular Biology, University College London, London WC1E 6BT, UK
3. National Physical Laboratory, Hampton Road, Teddington TW11 0LW, UK
4. Department of Molecular Biology, Princeton University, Princeton, New Jersey, USA
5. Department of Biochemistry, South Parks Road, University of Oxford, Oxford OX1 3QU, UK
6. Department of Physics and Astronomy, University College London, WC1E 6BT London, UK
7. Institute for the Physics of Living Systems, University College London, WC1E 6BT London, UK
8. MRC Laboratory for Molecular Cell Biology, University College London, WC1E 6BT London, UK
9. Department of Physics, King's College London, Strand Lane, London WC2R 2LS, UK

\* Corresponding authors: colin.kleanthous@bioch.ox.ac.uk, tsilhavy@princeton.edu,  
b.hoogenboom@ucl.ac.uk

### Author Contributions

G.B. designed experiments, carried out and analysed AFM measurements, and wrote the initial draft of the paper. I.V.M. prepared mutant strains, carried out biochemical analyses and advised on the interpretation of the AFM experiments. P.G.I. carried out and analysed single-particle tracking experiments and advised on the interpretation of the AFM experiments. J.C.F. designed image analysis protocols and wrote analysis software. N.O. wrote analysis software. C.B. carried out and analysed nanomechanical experiments. M.G.R. conceived the study and supervised research. C.K. conceived the study, designed experiments, advised on their interpretation and supervised research. T.J.S. conceived the study, designed experiments, advised on their interpretation and supervised research. B.W.H. conceived the study, designed experiments, advised on their interpretation, wrote the initial draft of the paper and supervised research. All authors provided feedback on the data and interpretation, and input into the writing of the manuscript.

### Competing interest statement

The authors declare no competing interests

### Classification

Biological sciences: Microbiology

Physical sciences: Biophysics and Computational Biology

### Keywords

Gram-negative bacteria, outer membrane, phase separation, atomic force microscopy.

## 1 **Abstract**

2 Gram-negative bacteria are surrounded by a protective outer membrane (OM) with phospholipids in  
3 its inner leaflet and lipopolysaccharides (LPS) in its outer leaflet. The OM is also populated with many  
4  $\beta$ -barrel outer membrane proteins (OMPs), some of which have been shown to cluster into  
5 supramolecular assemblies. However, it remains unknown how abundant OMPs are organised across  
6 the entire bacterial surface and how this relates to the lipids in the membrane. Here we reveal how  
7 the OM is organised from molecular to cellular length scales, using atomic force microscopy (AFM) to  
8 visualise the OM of live bacteria, including engineered *Escherichia coli* (*E. coli*) strains and  
9 complemented by specific labelling of abundant OMPs. We find that a predominant OMP in the *E. coli*  
10 OM, the porin OmpF, forms a near-static network across the surface, which is interspersed with barren  
11 patches of LPS that grow and merge with other patches during cell elongation. Embedded within the  
12 porin network is OmpA, which forms non-covalent interactions to the underlying cell wall. When the  
13 OM is destabilised by mislocalisation of phospholipids to the outer leaflet, a new phase appears,  
14 correlating with bacterial sensitivity to harsh environments. We conclude that the OM is a mosaic of  
15 phase-separated LPS-rich and OMP-rich regions, the maintenance of which is essential to the integrity  
16 of the membrane and hence to the lifestyle of a Gram-negative bacterium.

## 17 **Significance Statement**

18 Antimicrobial resistance is particularly prevalent in Gram-negative bacteria, as antibiotics that act  
19 inside the cells must overcome their outer membrane. So far, technical limitations have prevented us  
20 from determining how outer membrane proteins and lipids are organised to form this functional  
21 barrier. Here, we use nanoscale imaging of live bacteria to reveal that the most abundant outer  
22 membrane proteins form a network that spans the entire bacterial surface, leaving only small gaps of  
23 phase-separated lipopolysaccharide. This tendency to phase-separate is further emphasised by the  
24 formation of new domains when phospholipids are mislocated at the surface, rendering cells more  
25 susceptible to some antibiotics. Overall, the phase-separated nature of the outer membrane defines  
26 a new perspective on its integrity and barrier function.

## 27 **Main Text**

### 28 **Introduction**

29 Diderm bacteria such as *E. coli* are surrounded by an outer membrane (OM) that protects cells against  
30 the immune systems of plants and animals, contributes to the mechanical stability of the cell and  
31 excludes many classes of antibiotics thereby contributing to antimicrobial resistance (1, 2). The OM is  
32 comprised of an asymmetric bilayer of phospholipids in the inner leaflet, lipopolysaccharides (LPS) in  
33 the outer leaflet and many outer membrane proteins (OMPs). OMPs are hugely diverse  $\beta$ -barrel  
34 proteins that can be present at 100s to 100,000s copies per cell (3). They have been shown to be  
35 relatively static (4), probably due to promiscuous protein-protein interactions and binding of LPS that  
36 exists in a slow moving, liquid-crystalline state (5, 6). Using fluorescent labels, some OMPs have been  
37 shown to cluster into supramolecular islands of  $\sim 0.3$ - $0.5 \mu\text{m}$  sizes (4, 7–9). However, it remains  
38 unknown how abundant OMPs are organised across the entire bacterial surface and how this relates  
39 to the lipids in the membrane.

40 To address this fundamental question, we have imaged the entire surface of live and metabolically  
41 active bacteria at nanometre resolution, using AFM. Applying such large-scale, high-resolution imaging  
42 on engineered *E. coli* strains and complementing it by specific labelling of abundant OMPs, we identify  
43 large-scale and near-static protein-rich networks interspersed with nanoscale domains that are  
44 enriched in LPS. Key components of the protein-rich networks are abundant trimeric porins such as  
45 OmpF, in addition to (the monomeric) OmpA, which forms non-covalent interactions to the underlying  
46 cell wall (10). By contrast, no significant protein content is detected in the LPS-rich domains, which are

1 also found to grow and merge with other patches during cell elongation. When the LPS-phospholipid  
2 asymmetry of the OM is perturbed by mislocalisation of phospholipids to the outer leaflet (11), we  
3 find deformation of the membrane rather than expansion of LPS patches, indicating the appearance  
4 of a new, phospholipid-enriched phase at the bacterial surface.

## 5 **Results**

### 6 **Identification of networks of trimeric porins spanning the bacterial surface**

7 To resolve the supramolecular organisation of the unlabelled OM in live bacteria, *E. coli* were  
8 immobilised onto glass coverslips and imaged by AFM in minimal media (12, 13). AFM images labelled  
9 'phase' represent the variation in the phase of the oscillating AFM probe, which depends on local  
10 material properties (14). In contrast to the simultaneously acquired surface topography (height), the  
11 phase allowed us to view molecular-scale detail against a background that was less affected by  
12 variations of the surface topography seen at cellular length scales. At a low magnification, cells had a  
13 smooth appearance (Fig. 1A). By recording multiple higher-magnification scans and overlaying these  
14 to obtain a cell-wide, molecular-scale map of the accessible OM, the bacterial surface was shown to  
15 contain a dense packing of pores, superposed to a background with 2-5 nm height variations at a ~50  
16 nm length scale (Fig. 1B-C and Supplementary Fig. S1A).

17 To aid the assignment of the observed pore structures, each pore was localised and the pore packing  
18 quantified via the nearest-neighbour distance (~9 nm) and angular distribution of near neighbours  
19 (peaked just below 60°; Supplementary Fig. S1B-C). This is locally consistent with the hexagonal  
20 lattices of porin trimers reconstituted in lipid membranes (15–20), with one observable pore for each  
21 trimer. The ~8 nm diameter of observed pores also fits well with the dimensions from crystal  
22 structures of trimeric porins (21). We therefore attributed the pore network to trimeric porins. This  
23 interpretation was confirmed by modulation of the expression of the most abundant trimeric porins,  
24 OmpF and OmpC, via the removal and reintroduction of their transcriptional activator, OmpR (22) (Fig.  
25 1D). This removal greatly reduced the number of pores per unit area ( $\mu\text{m}^2$ ) and its reintroduction led  
26 to increasing amounts of pores (Fig. 1E-F), showing similar trends as the *ompF* and *ompC* expression  
27 (Fig. 1D). Similar results were also obtained on a different *E. coli* strain without trimeric porins OmpF,  
28 OmpC and LamB, where cells had no pore features in AFM images (Supplementary Fig. S1A),  
29 confirming that the observed pores correspond to trimers of porins. This was independent of LPS  
30 levels, as these were not affected by the removal of trimeric porins (Supplementary Fig. S1D,E).

31 The pores in these cell-wide networks showed very low mobility: by AFM, we found a low median  
32 diffusion coefficient of  $2 \times 10^{-7} \mu\text{m}^2 \text{ s}^{-1}$ . By single-molecule fluorescence microscopy, the median  
33 diffusion coefficient of OmpF was measured (at lower spatial resolution) as  $0.0018 \mu\text{m}^2 \text{ s}^{-1}$  for live cells,  
34 not significantly higher than control experiments on fixed cells (Supplementary Fig. S2). The crowded  
35 and static nature of this trimeric porin network is remarkable as the OM expands and rearranges at  
36 cellular length scales during growth.

### 37 **Lipopolysaccharide patches provide openings in the proteinaceous network**

38 Presuming that membrane biogenesis implies a substantial supramolecular rearrangement and the  
39 ready formation of defects, the dense porin network was inspected for interruptions. By imaging the  
40 whole cell, sparse, pore-free, smooth patches were revealed, protruding by ~0.5-1 nm above the pore  
41 network (Fig. 2A-B). The patches are ~25-225 nm wide, with a mean diameter of 55 nm, and were  
42 found on all cells. We note the similarity of these observations to early freeze-fracture electron  
43 microscopy images (23–26), yet here we consistently observed such patches on live and dividing  
44 bacteria (Supplementary Fig. S3A-B). Strikingly, patches appeared to behave as liquid phases in the  
45 membrane: merging, growing and splitting apart over long time periods, but maintaining their  
46 approximate lateral positions at the bacterial surface (Fig. 2C and Supplementary Fig. S3C-D).

1 The lack of pores in smooth OM patches suggests that they have a low protein content. To verify this,  
2 we specifically labelled trimeric OmpF and monomeric OmpA as they are two of the most abundant  
3 OMPs in *E. coli*, each present at ~100,000 copies per cell (2, 27, 28). OmpF trimers were labelled by  
4 colicin N<sup>1-185</sup>mCherry, which binds OmpF with high affinity (29). The diameter of the mCherry is ~3.5  
5 nm (30): this is large enough to prevent entry into the porin and to thus block the translocation of the  
6 fused colicin through the OmpF, leaving the colicin N<sup>1-185</sup>mCherry fusion in a partially translocated,  
7 tightly bound state. Importantly, it is also large enough to make it readily detectable via protrusions  
8 in the AFM height images. This allows the localisation of mCherry molecules to single nanometre  
9 resolution by AFM, without relying on fluorescence microscopy (Fig. 2D). These labels are poorly  
10 resolved in the AFM phase images of the same area, but in phase images the patches are more easily  
11 distinguished and marked. This allowed the independent, unbiased detection of labels and patches.  
12 mCherry labels were found to localise only to the pore networks.

13 For OmpA, we used a similar AFM-based localisation of a globular protein in the height images: *E. coli*  
14 MG1655 expressing *ompA* with a streptavidin-binding peptide in an outer loop (31) were labelled with  
15 streptavidin (Fig. 2E). The OmpA labels also co-localised with the pore networks, and not with patches  
16 (Fig. 2E). Both for OmpF and OmpA labels, the co-localisation with patches was at or below the noise  
17 floor due to false positives (Supplementary Fig. S4), suggesting that patches are largely or totally  
18 devoid of protein. This conclusion is further supported by the observation of smoother, presumably  
19 protein-free patches against a rougher background in cells without OmpF and OmpC, with the  
20 roughness of the background assumed to be due to other OMPs (Supplementary Fig. S5). Taken  
21 together, our data demonstrates that distinct nanoscale, protein-poor domains are phase-separated  
22 from densely packed proteinaceous areas in the OM, and gradually change during growth.

23 Since OMPs have been shown to readily interact with LPS by the structural resolution of LPS-OMP  
24 complexes (32, 33), it is likely that LPS is found throughout the membrane, including the pore network.  
25 However, because the smooth patches contained no detectable protein in our AFM studies, we  
26 hypothesised that they are instead enriched in or dominated by excess LPS. Therefore, larger  
27 expression levels of LPS were expected to lead to a larger part of the bacterial surface being covered  
28 by patches. To test this, the levels of LPS were modulated by altering the efficiency of LpxC (34),  
29 involved in the synthesis of lipid A in LPS (Fig. 3A). Increasing LPS production led to a significantly  
30 increased fraction of the bacterial surface being covered by smooth patches (Fig. 3B and  
31 Supplementary Fig. S6A), whereas the overall morphology of the patches and packing of the pore  
32 network remained the same (Fig. 3C-E and Supplementary Fig. S6B and S7A-B). The decrease in patch  
33 area with low LPS levels also coincided with an increase in pore density (Supplementary Fig. S6C) and  
34 slight decrease in mean patch size (Fig. 3C). The fact that the patch area is dependent on LPS  
35 abundance provides evidence that these patches are phase separated, LPS-enriched domains.

36 If patches are indeed LPS-enriched phases, their phase separation from the proteinaceous network  
37 should be increased by promoting LPS-LPS interactions (compared with LPS-protein interactions).  
38 MG1655 have no O-antigen, so LPS are primarily bound together by Mg<sup>2+</sup>, which strongly bridges the  
39 negatively charged LPS core (2). By reintroducing *wbbL*, the O-antigen is restored and the long  
40 polysaccharide chains enhance LPS-LPS interactions (35, 36). We predicted this would lead to a  
41 significant increase in typical patch size (area per patch) and this was indeed the case, with typical  
42 patch sizes notably exceeding those for WT (Fig. 3C, MG1655 vs +*wbbL*, and Supplementary Fig. S6A).

43 Since the size of patches is dependent on LPS content and interaction strength, we conclude that they  
44 are indeed LPS-enriched. Furthermore, reported diffusion of LPS is slow (37, 38) which is consistent  
45 with gradual changes observed for the LPS-enriched patches (Supplementary Fig. S3C-D).

#### 46 **Externalised phospholipids break the porin network to form new domains**

47 Finally, the observation of LPS patches and protein-rich networks raises the question of how these  
48 arrangements are affected by phospholipids in the outer leaflet, which represent a disruption of the

1 lipid asymmetry and lead to increased sensitivity towards detergents and the antibiotic bacitracin (39)  
2 (Supplementary Fig. 8A). Phospholipids are usually restricted to the inner leaflet by the Mla pathway  
3 and the phospholipase PldA: the combined deletion of *pldA* and disruption of the Mla pathway results  
4 in a ~25 fold enhancement of phospholipids in the outer leaflet, compared with WT (11). This double  
5 deletion severely disrupts the OM permeability barrier rendering the mutant strain sensitive to  
6 moderate concentrations of SDS-EDTA, as opposed to single *pldA* or *m1aA* deletions, which are as  
7 resistant as WT under those conditions (11) (Supplementary Fig. S8A).

8 Consistent with this physiological behaviour, the morphology of the single  $\Delta m1aA$  or  $\Delta pldA$  mutants  
9 did not differ significantly from WT in our AFM assays, whereas  $\Delta m1aA \Delta pldA$  double mutant cells  
10 showed substantial changes in their OM architecture (Fig. 4A-B). The  $\Delta m1aA \Delta pldA$  OMs showed  
11 abundant, high (~2 nm), pore-free protrusions, here referred to as phospholipid-enriched patches (Fig.  
12 4). The phospholipid-enriched patches are distinct from LPS-enriched patches by this greater  
13 protrusion (height) and by their shape (Fig. 4A).  $\Delta m1aA \Delta pldA$  patches were found to be smaller,  
14 reflected by a lower mean area per patch (Fig. 4E), and any large  $\Delta m1aA \Delta pldA$  patches were elongated,  
15 shown by a higher patch aspect ratio (Fig. 4F). Additional evidence that phospholipids form new  
16 patches is seen as LPS-enriched patches were observed alongside the abundant phospholipid-  
17 enriched patches on  $\Delta m1aA \Delta pldA$  cells (Supplementary Fig. S9).

## 18 Discussion

19 The lateral organisation of OMPs and lipids provides important context for understanding their  
20 insertion into the OM (40) and more generally the architectural features that underpin OM function.  
21 For some OMPs, fluorescence microscopy has shown how promiscuous protein-protein interactions  
22 can lead to non-homogenous patterning across the cell into OMP islands (4, 7–9, 41). In contrast, our  
23 results reveal an entirely different type of supramolecular organisation in which an OMP network  
24 spans the entire bacterial surface and is only interrupted by nanoscale domains that are depleted of  
25 common OMPs and enriched in LPS.

26 Here, observed on live and metabolically active bacteria, the dense packing of OMPs is consistent with  
27 older electron microscopy data on freeze-fractured bacteria, which show the OM covered in proteins  
28 (23–26, 42). In addition, it is consistent with previous AFM results on small outer membrane areas (12,  
29 43–45) and on isolated OMs (46), which show similar arrangements of densely packed proteins at a  
30 local scale. Seen in the light of these previous results, our data provide further evidence that copies of  
31 abundant proteins (OmpF, OmpC and OmpA) do not form isolated islands, but fill the membrane with  
32 an imperfect protein lattice from pole to pole (Fig. 1). Of note, this does not preclude the existence –  
33 within the network – of islands of OMPs that, e.g., have been synthesised or inserted at similar  
34 timepoints (4).

35 Although consistent with previous AFM analyses (44) and with single-molecule fluorescence  
36 microscopy of labelled OmpF (4, 27, 47), a puzzling aspect of this protein network is the near-static  
37 appearance of its constituents, since it raises the question of how the OM accommodates growth (4,  
38 8, 27, 47, 48). Based on the results reported here, we speculate that LPS-enriched, OMP-depleted  
39 regions may facilitate insertion of new membrane components.

40 In addition to phase-separated LPS patches, different domains appear when phospholipids are present  
41 in the outer leaflet (Fig. 4), as here resulting from the combined deletion of *pldA* and disruption of the  
42 Mla pathway (11). These presumably phospholipid-enriched domains appear in the OMP network,  
43 separate from the LPS domains. Their appearance is found to directly correlate with bacterial  
44 sensitivity to harsh environments, demonstrating a link between OM phase-separation and functional  
45 behaviour of Gram-negative bacteria, and explaining this enhanced sensitivity as due to local defects  
46 in the LPS-OMP dominated outer leaflet of the OM. The distinction between LPS-enriched patches and  
47 phospholipid-enriched patches is consistent with earlier evidence that LPS and phospholipids do not  
48 mix in the OM (49). It may also rationalise the association of MlaA with OmpC and OmpF in the OM

1 (50), as this association could direct MlaA to the porin network where the externalised phospholipids  
2 emerge (*i.e.*, not in the LPS patches), to sense local OM disruption and activate retrograde transport  
3 of phospholipids to the inner membrane (11).

4 Taken together, these results represent the highest-resolution microscopy data of live cells reported  
5 to-date and define the supramolecular architecture of the *E. coli* OM. Importantly, they provide a  
6 framework within which to understand associations between different OMPs, LPS and phospholipids  
7 in the OM. Finally, this framework also provides a perspective to assess how bacterial sensitivity to  
8 immune effectors and antimicrobials may depend on local as well as global properties of the OM.

## 9 **Materials and Methods**

10 **Bacterial strains and growth conditions.** All strains are shown in Supplementary Table S1. Unless  
11 otherwise stated, strains were constructed by generalized P1 transduction or transformation in *E. coli*  
12 strain MG1655 (51). Null alleles were obtained from the Keio collection (52) and FRT-flanked  
13 kanamycin resistance cassette was removed using the Flp recombinase system, as previously  
14 described (53). O-antigen was restored by introducing a wild-type copy of the *wbbL* gene at the native  
15 chromosomal locus. Production of O-antigen was assayed as gain of resistance against P1 phage (54).  
16 For AFM, bacteria were grown overnight in LB broth at 37 °C, diluted 100x into fresh LB and incubated  
17 for 2.5 more hours for exponentially growing cells. Where appropriate, LB was supplemented with  
18 100 µg/ml ampicillin, 50 µg/ml kanamycin, 10 µg/ml tetracycline, 0.5% arabinose, 0.5% glucose and  
19 0.1% fucose.

20 **Plasmid construction:** The plasmids used in this study are listed in Supplementary Table S2. To  
21 construct pBAD18::*ompR*, polymerase chain reaction was used to amplify the plasmid using  
22 oligonucleotides IMB89:pBAD18\_openF (gaattcgagctcgggtacc) and IMB90:pBAD18\_openR  
23 (gctagcccaaaaaaacgg) and the *ompR* open reading frame using oligonucleotides  
24 IMB93:ompR\_pBAD18F(acccgttttttgggctagctcacacaggaagggtggcatgcaagagaactac) and  
25 IMB94:ompR\_pBAD18R(cgggtaccgagctcgaattctcatgcttagagccgtc). Products were purified using  
26 QIAquick PCR purification kit (Qiagen) and assembled using Gibson Assembly (NEB).

27 **Immunoblot Analysis.** OD<sub>600</sub> 1.0 exponentially growing cells were collected and lysed in 50 µl 2X  
28 Laemelli sample buffer (Bio-Rad) supplemented with β-mercaptoethanol (Sigma-Aldrich) by boiling for  
29 10 minutes. 8 µl of sample was loaded and electrophoresed on a 10% SDS-PAGE gel. Proteins and LPS  
30 were transferred onto a nitrocellulose membrane using the Trans-Blot Turbo Transfer System (Bio-  
31 Rad). Membranes were blocked for 1 hr in 5% milk at 4 °C, followed by incubation with primary  
32 antibody probing for αOmpF/C (1:10,000), αLPS (1:5,000; Hycult Biotech), or αGroEL (1:50,000; Sigma-  
33 Aldrich) overnight at 4 °C. Goat anti-rabbit IgG horseradish peroxidase (1:10,000; Sigma-Aldrich) or  
34 goat anti-mouse horseradish peroxidase (1:10,000; Bio-Rad) secondary antibodies were incubated for  
35 1 hr at room temperature.

36 **OmpF photoactivated localisation microscopy single particle tracking (PALM-SPT).** PALM-SPT was  
37 conducted on an Oxford Nanoimaging Ltd. Nanoimager S with a 100x, 1.49 NA objective. Overnight  
38 culture of MG1655 grown in M9 glucose (M9 minimal media + 0.05% (w/v) casamino acids, 0.4% D-  
39 glucose, 2 mM MgSO<sub>4</sub>, 0.1 mM CaCl<sub>2</sub>) was transferred to 4 ml fresh M9 glucose and grown to an OD<sub>600</sub>  
40 of 0.6 – 0.9. A volume of cells equivalent to 500 µl of OD<sub>600</sub> 0.6 culture was pelleted and resuspended  
41 in 200 µl fresh M9 glucose supplemented with 200 nM colicin N<sup>1-185</sup>PAmCherry (expressed and purified  
42 in the same manner as colicin N<sup>1-185</sup>mCherry (29)), labelling of OmpF was allowed to proceed at room  
43 temperature for 10 minutes on a rotary shaker. Labelled cells were either fixed or prepared live for  
44 microscopy. Fixation was conducted by resuspension of a labelled cell pellet in 1 ml 4% formaldehyde  
45 for 30 minutes at 4 °C. Prior to loading cells onto slides, excess label was removed by 4 rounds of  
46 pelleting and resuspension (in PBS for fixed cells and M9 glucose for live cells). 4 µl of cells were loaded  
47 onto 1 % agarose PBS pads and imaged. Room temperature PALM-SPT was conducted, and the data  
48 analysed as described in reference (55).

1 **Coverslip preparation for AFM.** 13 mm glass coverslips (VWR) were sonicated in a 1-2% SDS solution  
2 in a Fisherbrand™ bath sonicator (Fisher Scientific) at 37 kHz and 100% power for 10 minutes. They  
3 were then rinsed in milliQ water (mQ), then ethanol, dried with nitrogen and plasma cleaned in air at  
4 70% power for 2 minutes. The whole procedure was then repeated. To ensure bacteria adhered to  
5 coverslips, they were soaked in a 50:1 solution of Acetone:Vectabond® (Vector Laboratories, USA) for  
6 5 minutes, rinsed in mQ and dried with nitrogen. Vectabond® coated coverslips were glued to clean  
7 glass slides using biocompatible glue (Reprorubber thin pour, Flexbar, NY) and were not stored (12).

8 **Preparation of cells for AFM.** For all AFM, except where specified otherwise, bacteria were prepared  
9 as follows. Freshly grown bacteria were washed 3 times by spinning for 2 minutes at 5,000 rpm and  
10 resuspending in minimal media (MM; 1X M9 salts (ThermoFisher), 2 mM MgSO<sub>4</sub>, 0.1 mM CaCl<sub>2</sub>, 0.36%  
11 glucose). 100 µl of washed cells were then resuspended in 20 mM HEPES and immediately applied to  
12 a Vectabond® coated coverslip for 5 minutes to adhere. For mechanical measurements, bacteria were  
13 resuspended in MM and applied to the coverslip for 30 minutes. The slide was then washed 3 times  
14 with 1 ml MM to remove unadhered bacteria and exchange buffers. With ~100 µl volume on the  
15 coverslip, ~5 µM SYTOX™ Green nucleic acid stain (Sigma-Aldrich) was added and incubated at room  
16 temperature for at least 5 minutes.

17 For streptavidin labelling, MG1655 pGV28 OmpA-SA1 cells (described in reference (31)) were induced  
18 with 2.2 mg/ml IPTG for 1 hour during the 2.5-hour growth. They were then washed 3 times in PBS  
19 and 100 µl was applied to a Vectabond® coated coverslip for 30 minutes. The coverslip was washed 3  
20 times with PBS and SYTOX™ was added. When using streptavidin, 10 µg/ml was added and incubated  
21 on the slide for 30 minutes. SYTOX™ was then reapplied.

22 For colicin N<sup>1-185</sup>mCherry labelling, exponential cells were washed 3 times by spinning for 1 minute at  
23 7,000 g and resuspending in minimal media 0.4% (MM 0.4%: 1X M9 salts, 2 mM MgSO<sub>4</sub>, 0.1 mM CaCl<sub>2</sub>,  
24 0.4% glucose). Cells were resuspended at OD<sub>600</sub> 0.5. 250 µl bacteria were then spun, resuspended in  
25 MM 0.4% with 0.1 µM Colicin N<sup>1-185</sup>mCherry (unlabelled controls were resuspended in MM 0.4%) and  
26 incubated at room temperature on a rotary shaker for 5 minutes. Labelled cells were then washed  
27 with MM 0.4% 3 times by spinning and resuspending. Then, cells were resuspended in 100 µl 20 mM  
28 HEPES, applied to a Vectabond® coated coverslip for 5 minutes and washed 3x with 1 ml MM 0.4%.

29 **Atomic Force Microscopy.** All AFM was performed on a Nanowizard III AFM with UltraSpeed head  
30 (Bruker AXS, CA, USA) with an Andor Zyla 5.5 USB3 fluorescence camera on an Olympus IX 73 inverted  
31 optical microscope. AFM imaging was performed in AC mode with a FastScanD cantilever. The drive  
32 frequency was 90-140 kHz, depending on the cantilever resonance, with a setpoint of 5-15 nm (50-  
33 70% relative to free amplitude). The whole cell image in Figure 1 was acquired at 2 Hz, 2.5 µm square  
34 and 512 pixels. All other AC mode images are 500 nm and 512 pixels square, recorded at 2-8 Hz.

35 Mechanical measurements were performed in QI™ mode with a FastScanD (Bruker AXS, CA, USA)  
36 cantilever (0.25 N/m nominal spring constant and 110 kHz resonant frequency). For mechanical  
37 measurements, deflection sensitivity was calibrated by indenting cantilevers on glass up to a peak  
38 force of 0.2 nN with a 1 µm z-length, next the cantilever stiffness was calibrated by measuring the  
39 thermal noise of the cantilever. 500 nm scans were then taken on the surface of bacteria with 128x128  
40 pixels, 0.1 nN setpoint, 90 nm z-length and 30 µm s<sup>-1</sup> z-speed.

41 **AFM force curve and image processing.** QI™ mode images were analysed in the JPK data processing  
42 software. The effective Young's modulus was calculated using the Hertz-Sneddon model assuming a  
43 paraboloid tip shape, a radius of 2 nm and a Poisson ratio of 0.5. Final images were imported into  
44 Gwyddion 2.52 (<http://gwyddion.net/>) (56) and the colour scale set.

45 Figure 1a was not post-processed but the colour scale was set in Gwyddion. Small images were first  
46 processed with a Python script using Pygwy (from Gwyddion (56)) and originally adapted from AFM-  
47 SPM/TopoStats (57). The script took Height and Phase channels of each image, applied a first order

1 polynomial fit to align rows and exported the file as a text image. A custom FIJI-ImageJ (58) macro  
2 imported the text image, applied a highpass filter (1-50 pixels, with 0.97 nm per pixel) to remove  
3 curvature of the cell and a 1 pixel gaussian smoothing to reduce noise. Gwyddion was used for image  
4 representation and height profiles. Further analysis was performed as described below.

5 **Localisation of labels.** Masks of patch regions were marked manually in FIJI-ImageJ using the phase  
6 channel because labels were poorly visible in the phase, meaning potential bias would be reduced.  
7 Labels were found by applying a highpass filter (1-20 pixels, with 0.97 nm per pixel) and a 2 pixel  
8 gaussian blur to the height channel, then finding maxima with a prominence of 0.5 nm using a peak-  
9 search algorithm (the Find Maxima function in FIJI-ImageJ). The number of labels per  $\mu\text{m}^2$  in patch and  
10 network areas were calculated in MATLAB (Mathworks).

11 **Pore and patch analysis.** For high-resolution whole-cell images required for pore and patch finding,  
12 500 nm scans were performed across the bacterial surface. The approximate location of each scan is  
13 recorded in the jpk file and was accessed in the JPK data processing software. Individual phase scans  
14 were then accurately overlaid in FIJI-ImageJ by comparing surface features in each image. Once  
15 overlays covering the accessible cell surface were complete, a mask of patches was generated by  
16 manually marking patch edges in FIJI-ImageJ. Any patch less than about  $400\text{ nm}^2$  was ignored as their  
17 identification was often ambiguous. To calculate the relative patch area, the area of bacterial surface  
18 imaged was outlined manually and the percentage imaged area taken up by patches was calculated in  
19 MATLAB (Mathworks). The FIJI-ImageJ shape descriptors function was used to find patch aspect ratios  
20 and individual patch areas.

21 For pore locations, the Find Maxima function in FIJI-ImageJ was first used to find potential pores. Any  
22 points that fell outside the imaged area were ignored and the remaining points exported as  
23 coordinates. The Enhance Local Contrast (CLAHE) function was then used to normalise contrast across  
24 the surface, since contrast was usually higher at the edges of cells. Uncorrected, this led to central  
25 pores being missed. The corrected image was exported as an 8-bit with potential pore coordinates.  
26 Actual pores were then found using a machine learning model described below. Nearest neighbour  
27 and angular distributions were determined using custom MATLAB scripts (available at  
28 <https://github.com/hoogenboom-lab/image-analysis>). For angular distributions, neighbours less than  
29 15 nm were found for each pore and the angle between each of these neighbours, with respect to the  
30 centre pore, was found.

31 For diffusion analysis, time-lapse images were recorded at 91 seconds per frame for 20 minutes. Crops  
32 were taken of different locations within the image and pores identified and tracked manually from  
33 frame to frame. For each pair of pores at positions  $r_i$  and  $r_j$ , the autocorrelation function was calculated  
34  $\langle r_i(t)r_j(t+\tau) \rangle \approx -D\tau$ , where  $D$  is the diffusion coefficient and  $\tau$  is the delay time (59). The pore diffusion  
35 coefficient was then calculated from the slope of the autocorrelation function.

36 **Pore finding.** The labelling of pores in a cell image was performed using a machine learning model for  
37 object detection. A two-state image classifier was first developed to distinguish between images of  
38 pores and images of cell membrane where pores were not present. This model used a gradient  
39 boosted decisions trees method (60) with 50 weak learner models and used mean cross entropy as its  
40 loss function. Details of the method and a learning curve can be found in Supplementary Table S3 and  
41 Supplementary Fig. S10. The method was chosen based on its performance after multiple methods  
42 were tested by the Wolfram Mathematica Classify function (61).

43 The model was trained using a diverse set of cell images where pores had been labelled manually.  
44 Training data for the 'pore' class was generated by taking a  $9 \times 9$  pixel region around the manually  
45 labelled pore centre, while data from the 'not pore' class was generated by sampling the complement  
46 of the 'pore' regions and the original image. This produced a total dataset of 36,392 pore images and  
47 1,157,455 non-pore images, of these around 80% of each set were used for training and around 20%  
48 (235,267 images total) were held back for testing. To account for the imbalance between the minority



1 and majority class, the remaining pore class was oversampled to 10% of the majority class size,  
2 producing a final training set of 116,456 pore images and 925,964 non pore images (or 1,042,420  
3 images in total). A mosaic of a small sample of each class of the training set is provided in  
4 Supplementary Fig. S11A.

5 With this method, the classifier achieved an accuracy of 97.7% and an  $F_1$  score of 0.696. The confusion  
6 matrix from which these values are derived is given in Supplementary Fig. S11B. It is notable that the  
7 model's high accuracy may be skewed by the imbalance in the class sizes, and so cannot be considered  
8 a measure of performance when taken in isolation. The difficulty associated with the manual labelling  
9 of pores to be included in the training set may account for the low precision (the proportion of 'pore'  
10 predictions which were correct). By visual inspection of marked cells, the model found 90% of the  
11 pores present in images with few false positives, which was sufficiently accurate to label pores in real  
12 data.

13 To find pores in the data, the classifier was used as part of a scrolling window object detection routine  
14 where each 9x9 region around the pixels in a given region of a cell image were classified by the model.  
15 To reduce the region of the image to be sampled for classification, this was preceded by the step which  
16 identified the local brightness minima of the image where pores were most likely to appear and only  
17 the 11x11-pixel regions around these minima were checked by the scrolling window. This resulted in  
18 a set of labelled pixels for each image which were considered part of a pore (Supplementary Fig. S11C).  
19 These regions had a gaussian blur of radius 0.5 pixels applied in order to combine the labels of  
20 elongated or conjoined pores. The centroids of these regions were then found by applying image  
21 segmentation (via the Mathematica ComponentMeasurements function (62)), giving the final  
22 estimate of the centre point of the pores in the image. Using this method allowed for images to be  
23 labelled far more quickly than they would be manually, and with a greater accuracy than traditional  
24 image analysis approaches.

25 **Graphing and statistics.** All graphing and statistics were performed in OriginPro (OriginLab, MA, USA).  
26 Statistical tests are from a one-way ANOVA with Tukey's t-test and mean lines and standard deviations  
27 are shown in plots, unless otherwise stated.

## 28 **Acknowledgments**

29 We acknowledge Dr Richard Thorogate for technical support, Tanneke den Blaauwen for providing the  
30 pGV28 OmpA-SA1 plasmid and Guillermo Herrera-Sanchez for assistance with computational analysis.  
31 Research reported in this publication was funded by the UKRI BBSRC (BB/R000042/1 to B.W.H.), EPSRC  
32 (EP/N509577/1 to G.B. and B.W.H.; EP/K031953/1 for equipment via the IRC in Early-Warning Sensing  
33 Systems for Infectious Diseases), funding from the UK's Department for Business, Energy and  
34 Industrial Strategy (to G.B. and M.G.R.), and MRC (MR/R000328/1 to B.W.H.), and by the National  
35 Institute of General Medical Sciences of the National Institutes of Health under Award Numbers  
36 F32GM139232 (to I.V.M.) and R35-GM118024 (to T.J.S.). The content is solely the responsibility of the  
37 authors and does not necessarily represent the official views of the National Institutes of Health (or  
38 other funders). C.K. acknowledges funding for this work from the European Research Council  
39 (Advanced grant 742555; OMPorg). P.G.I. acknowledges studentship funding from the Medical  
40 Research Council UK.

## 41 **Data Availability**

42 Data supporting this study are available online, DOI: 10.5522/04/16547644.

## 43 **References**

- 44 1. E. R. Rojas, G. Billings, P. D. Odermatt, G. K. Auer, L. Zhu, A. Miguel, F. Chang, D. B. Weibel, J.  
45 A. Theriot, K. C. Huang, The outer membrane is an essential load-bearing element in Gram-  
46 negative bacteria. *Nature* **559**, 617–621 (2018).

- 1 2. T. J. Silhavy, D. Kahne, S. Walker, The bacterial cell envelope. *Cold Spring Harb Perspect Biol*  
2 (2010) <https://doi.org/10.1101/cshperspect.a000414> (January 29, 2019).
- 3 3. R. Koebnik, K. P. Locher, P. Van Gelder, Structure and function of bacterial outer membrane  
4 proteins: Barrels in a nutshell. *Mol. Microbiol.* **37**, 239–253 (2000).
- 5 4. P. Rassam, N. A. Copeland, O. Birkholz, C. Tóth, M. Chavent, A. L. Duncan, S. J. Cross, N. G.  
6 Housden, R. Kaminska, U. Seger, D. M. Quinn, T. J. Garrod, M. S. P. Sansom, J. Piehler, C. G.  
7 Baumann & C. Kleanthous. Supramolecular assemblies underpin turnover of outer membrane  
8 proteins in bacteria. *Nature* **523**, 333–336 (2015).
- 9 5. A. S. Ghosh, K. D. Young, Helical disposition of proteins and lipopolysaccharide in the outer  
10 membrane of *Escherichia coli*. *J. Bacteriol.* **187**, 1913–1922 (2005).
- 11 6. N. Paracini, L. A. Clifton, M. W. A. Skoda, J. H. Lakey, Liquid crystalline bacterial outer  
12 membranes are critical for antibiotic susceptibility. *Proc. Natl. Acad. Sci. U. S. A.* **115**, E7587–  
13 E7594 (2018).
- 14 7. G. Mamou, P. G. Inns, D. Sun, R. Kaminska, N. G. Housden, R. Cohen-Khait, H. Miller, K. M.  
15 Storek, S. T. Rutherford, J. Payandeh & C. Kleanthous, Spatiotemporal organization of BamA  
16 governs the pattern of outer membrane protein distribution in growing *Escherichia coli* cells.  
17 *bioRxiv*, 2021.01.27.428258 (2021).
- 18 8. S. D. Gunasinghe, T. Shiota, C. J. Stubenrauch, K. E. Schulze, C. T. Webb, A. J. Fulcher, R. A.  
19 Dunstan, I. D. Hay, T. Naderer, D. R. Whelan, T. D. M. Bell, K. D. Elgass, R. A. Strugnell & T.  
20 Lithgow, The WD40 Protein BamB Mediates Coupling of BAM Complexes into Assembly  
21 Precincts in the Bacterial Outer Membrane. *Cell Rep.* **23**, 2782–2794 (2018).
- 22 9. C. Kleanthous, P. Rassam, C. G. Baumann, Protein-protein interactions and the spatiotemporal  
23 dynamics of bacterial outer membrane proteins. *Curr. Opin. Struct. Biol.* **35**, 109–115 (2015).
- 24 10. R. N. Reusch, Insights into the structure and assembly of *Escherichia coli* outer membrane  
25 protein A. *FEBS J.* **279**, 894–909 (2012).
- 26 11. J. C. Malinverni, T. J. Silhavy, An ABC transport system that maintains lipid asymmetry in the  
27 Gram-negative outer membrane. *Proc. Natl. Acad. Sci. U. S. A.* **106**, 8009–8014 (2009).
- 28 12. G. Benn, A. L. Pyne, M. G. Ryadnov, B. W. Hoogenboom, Imaging live bacteria at the nanoscale:  
29 comparison of immobilisation strategies. *Analyst*, 1–15 (2019).
- 30 13. A. Viljoen, S. J. Foster, G. E. Fantner, J. K. Hobbs, Y. F. Dufrêne, Scratching the surface: bacterial  
31 cell envelopes at the nanoscale. *MBio* **11** (2020).
- 32 14. R. García, R. Pérez, Dynamic atomic force microscopy methods. *Surf. Sci. Rep.* **47**, 197–301  
33 (2002).
- 34 15. D. L. Dorset, A. Engel, M. Häner, A. Massalski, J. P. Rosenbusch, Two-dimensional crystal  
35 packing of matrix porin. *J. Mol. Biol.* **165**, 701–710 (1983).
- 36 16. H. J. Sass, G. Büldt, E. Beckmann, F. Zemlin, M. van Heel, E. Zeitler, J. P. Rosenbusch, D. L.  
37 Dorset & A. Massalski, Densely packed  $\beta$ -structure at the protein-lipid interface of porin is  
38 revealed by high-resolution cryo-electron microscopy. *J. Mol. Biol.* **209**, 171–175 (1989).
- 39 17. M. Simón, A. Mathes, A. Blanch, H. Engelhardt, Characterization of a porin from the outer  
40 membrane of *Vibrio anguillarum*. *J. Bacteriol.* **178**, 4182–4188 (1996).
- 41 18. F. A. Schabert, A. Engel, Reproducible acquisition of *Escherichia coli* porin surface topographs  
42 by atomic force microscopy. *Biophys. J.* **67**, 2394–2403 (1994).
- 43 19. F. A. Schabert, C. Henn, A. Engel, Native *Escherichia coli* OmpF porin surfaces probed by atomic  
44 force microscopy. *Science (80-. )*. **268**, 92–94 (1995).
- 45 20. J. P. Rosenbusch, Characterization of the Major Envelope Protein from *Escherichia coli*. *J. Biol.*

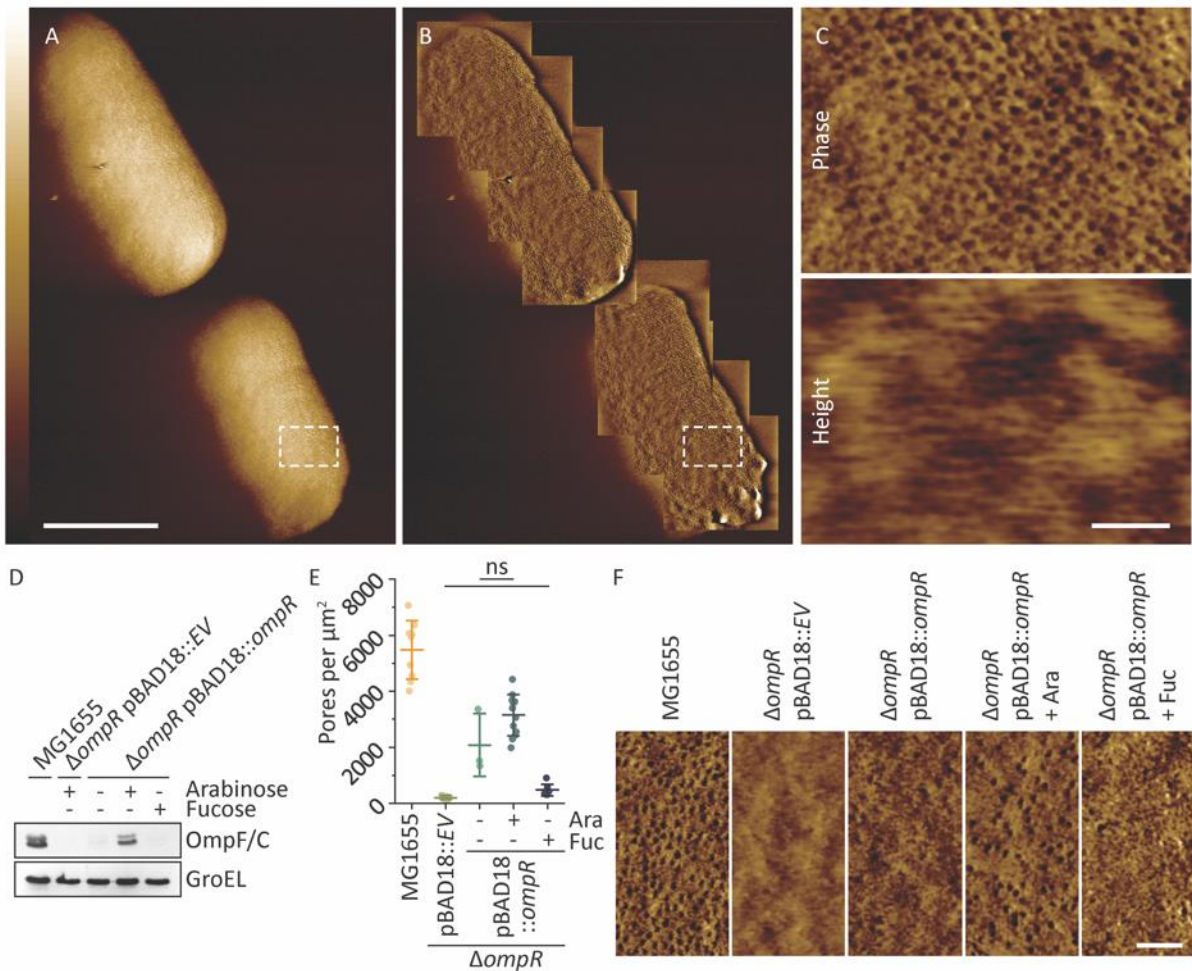
- 1 *Chem.* **249**, 8010–8029 (1974).
- 2 21. S. W. Cowan, R. M. Garavito, J. N. Jansonius, J. A. Jenkins, R. Karlsson, N. König, E. F. Pai, R. A.  
3 Pauptit, P. J. Rizkallah, J. P. Rosenbusch, G. Rummel & T. Schirmer, The structure of OmpF  
4 porin in a tetragonal crystal form. *Structure* **3**, 1041–1050 (1995).
- 5 22. R. K. Taylor, M. N. Hall, L. Enquist, T. J. Silhavy, Identification of OmpR: A positive regulatory  
6 protein controlling expression of the major outer membrane matrix porin proteins of  
7 *Escherichia coli* K-12. *J. Bacteriol.* **147**, 255–258 (1981).
- 8 23. M. E. Bayer, C. Remsen, Structure of *Escherichia coli* after freeze-etching. *J. Bacteriol.* **101**,  
9 304–313 (1970).
- 10 24. M. E. Bayer, L. Leive, Effect of ethylenediaminetetraacetate upon the surface of *Escherichia*  
11 *coli*. *J. Bacteriol.* **130**, 1364–1381 (1977).
- 12 25. L. Van Alphen, A. Verkleij, J. Leunissen Bijvelt, B. Lugtenberg, Architecture of the outer  
13 membrane of *Escherichia coli*. III. Protein-lipopolsaccharide complexes in intramembraneous  
14 particles. *J. Bacteriol.* **134**, 1089–1098 (1978).
- 15 26. U. Sleytr, M. J. Thornley, A. M. Glauert, Location of the fracture faces within the cell envelope  
16 of *Acinetobacter* species strain MJT/F5/5. *J. Bacteriol.* **118**, 693–707 (1974).
- 17 27. P. Rassam, K. R. Long, R. Kaminska, D. J. Williams, G. Papadacos, C. G. Baumann & C.  
18 Kleanthous, Intermembrane crosstalk drives inner-membrane protein organization in  
19 *Escherichia coli*. *Nat. Commun.* **9** (2018).
- 20 28. M. L. Ortiz-Suarez, F. Samsudin, T. J. Piggot, P. J. Bond, S. Khalid, Full-Length OmpA: Structure,  
21 Function, and Membrane Interactions Predicted by Molecular Dynamics Simulations. *Biophys.*  
22 *J.* **111**, 1692–1702 (2016).
- 23 29. K. B. Jansen, P. G. Inns, N. G. Housden, J. T. S. Hopper, R. Kaminska, S. Lee, C. V. Robinson, H.  
24 Bayley & C. Kleanthous. Bifurcated binding of the OmpF receptor underpins import of the  
25 bacteriocin colicin N into *Escherichia coli*. *J. Biol. Chem.* **295**, 9147–9156 (2020).
- 26 30. X. Shu, N. C. Shaner, C. A. Yarbrough, R. Y. Tsien, S. J. Remington, Novel chromophores and  
27 buried charges control color in mFruits. *Biochemistry* **45**, 9639–9647 (2006).
- 28 31. G. S. Verhoeven, S. Alexeeva, M. Dogterom, T. den Blaauwen, Differential bacterial surface  
29 display of peptides by the transmembrane domain of OmpA. *PLoS One* **4**, 6739 (2009).
- 30 32. A. D. Ferguson, E. Hofmann, J. W. Coulton, K. Diederichs, W. Welte, Siderophore-mediated  
31 iron transport: Crystal structure of FhuA with bound lipopolysaccharide. *Science* **282**, 2215–  
32 2220 (1998).
- 33 33. W. Arunmanee, M. Pathania, A. S. Solovyova, A. P. Le Brun, H. Ridley, A. Baslé, V. Van Den Berg  
34 & J. H. Lakey, Gram-negative trimeric porins have specific LPS binding sites that are essential  
35 for porin biogenesis. *Proc. Natl. Acad. Sci. U. S. A.* **113**, E5034–E5043 (2016).
- 36 34. R. L. Guest, D. S. Guerra, M. Wissler, J. Grimm, T. J. Silhavy, YejM modulates activity of the  
37 YciM/FtsH protease complex to prevent lethal accumulation of lipopolysaccharide. *MBio* **11**,  
38 1–13 (2020).
- 39 35. D. Jefferies, J. Shearer, S. Khalid, Role of O-Antigen in Response to Mechanical Stress of the *E.*  
40 *coli* Outer Membrane: Insights from Coarse-Grained MD Simulations. *J. Phys. Chem. B* **123**,  
41 3567–3575 (2019).
- 42 36. P. R. Reeves & M. M. Cunneen, Chapter 18 - Biosynthesis of O-antigen chains and assembly.  
43 in *Microbial Glycobiology* (ed. O. Holst, P. J. Brennan, M. von Itzstein, A. P. Moran) 319-335  
44 (Academic Press, 2010).
- 45 37. S. D. Gunasinghe, C. T. Webb, K. D. Elgass, I. D. Hay, T. Lithgow, Super-resolution imaging of

- 1 protein secretion systems and the cell surface of Gram-negative bacteria. *Front. Cell. Infect.*  
2 *Microbiol.* **7**, 220 (2017).
- 3 38. M. Schindler, M. J. Osborn, D. E. Koppel, Lateral diffusion of lipopolysaccharide in the outer  
4 membrane of *Salmonella typhimurium*. *Nature* **285**, 261–263 (1980).
- 5 39. M. Vaara, Antibiotic-supersusceptible mutants of *Escherichia coli* and *Salmonella*  
6 *typhimurium*. *Antimicrob. Agents Chemother.* **37**, 2255–2260 (1993).
- 7 40. J. E. Horne, D. J. Brockwell, S. E. Radford, Role of the lipid bilayer in outer membrane protein  
8 folding in Gram-negative bacteria. *J. Biol. Chem.* **295**, 10340–10367 (2020).
- 9 41. T. S. Ursell, E. H. Trepagnier, K. C. Huang, J. A. Theriot, Analysis of Surface Protein Expression  
10 Reveals the Growth Pattern of the Gram-Negative Outer Membrane. *PLoS Comput. Biol.* **8**,  
11 1002680 (2012).
- 12 42. B. Lugtenberg, L. V Alphen, Molecular Architecture and Functioning of the Outer Membrane  
13 of *Escherichia Coli* and other Gram-negative Bacteria. *Biochim. Biophys. Acta* **737**, 51–115  
14 (1983).
- 15 43. Z. Oestreicher, A. Taoka, Y. Fukumori, A comparison of the surface nanostructure from two  
16 different types of gram-negative cells: *Escherichia coli* and *Rhodobacter sphaeroides*. *Micron*  
17 **72**, 8–14 (2015).
- 18 44. H. Yamashita, A. Taoka, T. Uchihashi, T. Asano, T. Ando & Y. Fukumori, Single-molecule  
19 imaging on living bacterial cell surface by high-speed AFM. *J. Mol. Biol.* **422**, 300–309 (2012).
- 20 45. D. A. Heesterbeek, B. W. Bardoel, E. S. Parsons, I. Bennett, M. Ruyken, D. J. Doorduyn, R. D.  
21 Gorham, E. T. Berends, A. L. B. Pyne, B. W. Hoogenboom & S. H. M. Rooijackers, Bacterial  
22 killing by complement requires membrane attack complex formation via surface-bound C5  
23 convertases. *EMBO J.*, e99852 (2019).
- 24 46. S. Jarosławski, K. Duquesne, J. N. Sturgis, S. Scheuring, High-resolution architecture of the  
25 outer membrane of the Gram-negative bacteria *Roseobacter denitrificans*. *Mol. Microbiol.* **74**,  
26 1211–1222 (2009).
- 27 47. M. Chavent, A. L. Duncan, P. Rassam, O. Birkholz, J. Hélie, T. Reddy, D. Beliaev, B. Hambly, J.  
28 Piehler, C. Kleanthous & M. S. P. Sansom, How nanoscale protein interactions determine the  
29 mesoscale dynamic organisation of bacterial outer membrane proteins. *Nat. Commun.* **9**  
30 (2018).
- 31 48. A. Paraschiv, S. Hegde, R. Ganti, T. Pilizota, A. D. S. Šarić, Dynamic Clustering Regulates Activity  
32 of Mechanosensitive Membrane Channels. *Phys. Rev. Lett.* **124**, 048102 (2020).
- 33 49. H. Nikaïdo, Y. Takeuchi, S. I. Ohnishi, T. Nakae, Outer membrane of *Salmonella typhimurium*.  
34 Electron spin resonance studies. *BBA - Biomembr.* **465**, 152–164 (1977).
- 35 50. Z. S. Chong, W. F. Woo, S. S. Chng, Osmoporin OmpC forms a complex with MlaA to maintain  
36 outer membrane lipid asymmetry in *Escherichia coli*. *Mol. Microbiol.* **98**, 1133–1146 (2015).
- 37 51. T. Silhavy, M. Berman, L. Enquist, Experiments with gene fusions. *Cold Spring Harb. Lab. Cold*  
38 *Spring Harb. NY* (1984).
- 39 52. T. Baba, T. Ara, M. Hasegawa, Y. Takai, Y. Okumura, M. Baba, K. A. Datsenko, M. Tomita, B. L.  
40 Wanner & H. Mori, Construction of *Escherichia coli* K-12 in-frame, single-gene knockout  
41 mutants: The Keio collection. *Mol. Syst. Biol.* **2** (2006).
- 42 53. P. P. Cherepanov, W. Wackernagel, Gene disruption in *Escherichia coli*: TcR and KmR cassettes  
43 with the option of Flp-catalyzed excision of the antibiotic-resistance determinant. *Gene* **158**,  
44 9–14 (1995).
- 45 54. T. D. Ho, M. K. Waldor, Enterohemorrhagic *Escherichia coli* O157:H7 gal mutants are sensitive

- 1 to bacteriophage P1 and defective in intestinal colonization. *Infect. Immun.* **75**, 1661–1666  
2 (2007).
- 3 55. J. Szczepaniak, P. Holmes, K. Rajasekar, R. Kaminska, F. Samsudin, P. G. Inns, P. Rassam, S.  
4 Khalid, S. M. Murray, C. Redfield & C. Kleanthous, The lipoprotein Pal stabilises the bacterial  
5 outer membrane during constriction by a mobilisation-and-capture mechanism. *Nat.*  
6 *Commun.* **11**, 112–114 (2020).
- 7 56. D. Nečas, P. Klapetek, Gwyddion: An open-source software for SPM data analysis. *Cent. Eur. J.*  
8 *Phys.* **10**, 181–188 (2012).
- 9 57. J. G. Beton, R. Moorehead, L. Helfmann, R. Gray, B. W. Hoogenboom, A. P. Joseph, M. Topf &  
10 A. L. B. Pyne, TopoStats – A program for automated tracing of biomolecules from AFM images.  
11 *Methods* (2021) <https://doi.org/10.1016/j.ymeth.2021.01.008>.
- 12 58. J. Schindelin, I. Arganda-Carreras, E. Frise, V. Kaynig, M. Longair, T. Pietzsch, S. Preibisch, C.  
13 Rueden, S. Saalfeld, B. Schmid, J. Y. Tinevez, D. J. White, V. Hartenstein, K. Eliceiri, P. Tomancak  
14 & A. Cardona, Fiji: An open-source platform for biological-image analysis. *Nat. Methods* **9**,  
15 676–682 (2012).
- 16 59. B. Tränkle, D. Ruh, A. Rohrbach, Interaction dynamics of two diffusing particles: Contact times  
17 and influence of nearby surfaces. *Soft Matter* **12**, 2729–2736 (2016).
- 18 60. J. H. Friedman, Greedy Function Approximation: A Gradient Boosting Machine. *Ann. Stat.* **29**,  
19 1189–1232 (2001).
- 20 61. Wolfram Research (2014), Classify, Wolfram Language function,  
21 <https://reference.wolfram.com/language/ref/Classify.html> (updated 2020).
- 22 62. Wolfram Research (2010), ComponentMeasurements, Wolfram Language function,  
23 <https://reference.wolfram.com/language/ref/ComponentMeasurements.html> (updated  
24 2017).

25

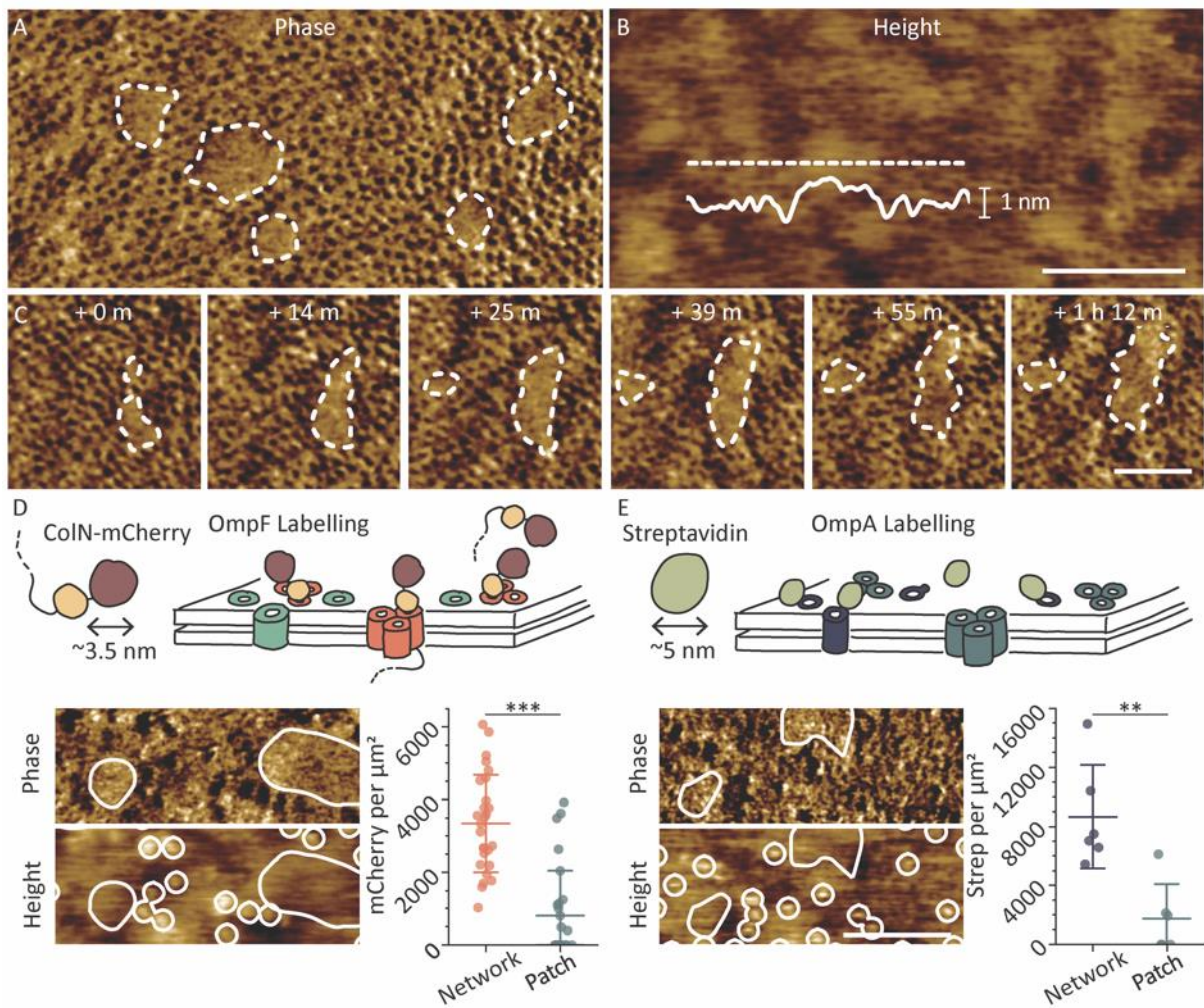
1

2 **Figures**

3

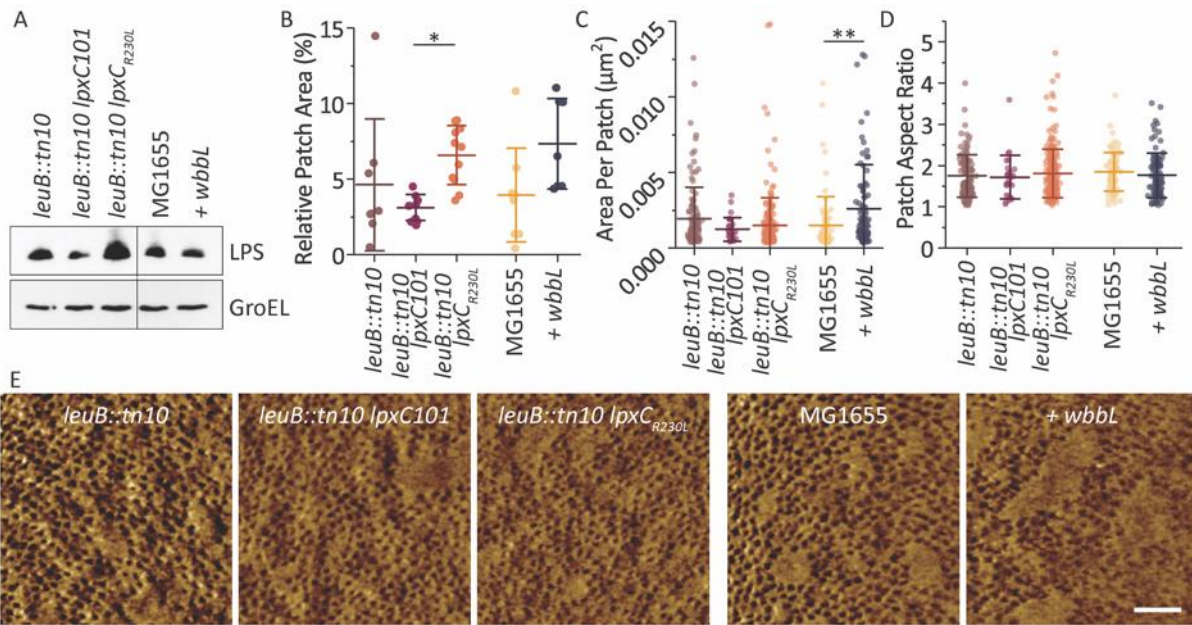
4 **Fig. 1. The OM contains a dense, crowded network of trimeric porins.** (A) Large AFM phase scans  
 5 show a MG1655 cell at low resolution and (B) images of the nanoscale architecture of the entire OM  
 6 can be produced by superimposing small, high-resolution phase images. (C) Enlarged phase and height  
 7 images, of the region marked by the dashed box in A-B, show the OM covered by a network of ~8 nm  
 8 wide pores. (D) Western blot showing variation in the levels of expression of OmpF and OmpC by the  
 9 removal of *ompR* and its reintroduction on an inducible plasmid. (E) Number of pores per  $\mu m^2$   
 10 detected in AFM images, showing that removal of *ompR* leads to the disappearance of the pores.  
 11 Subsequent reintroduction of *ompR* leads to an increase in pores with OmpF and OmpC expression.  
 12 Each data point corresponds to one cell with at least 3 independent experiments for each condition.  
 13 (F) Typical phase images used for the quantification in E. Horizontal scale bars are (A) 500 nm and (C)  
 14 and (F) 50 nm. Colour phase (measured in degrees) and height scales are (A) 7 deg, (B) 1.5 deg, (C) 1.5  
 15 deg and 5 nm, (F) 2 deg, 2 deg, 1 deg, 2 deg and 1 deg. ns =  $p > 0.5$ .

16



1  
2  
3  
4  
5  
6  
7  
8  
9  
10  
11  
12  
13  
14  
15  
16

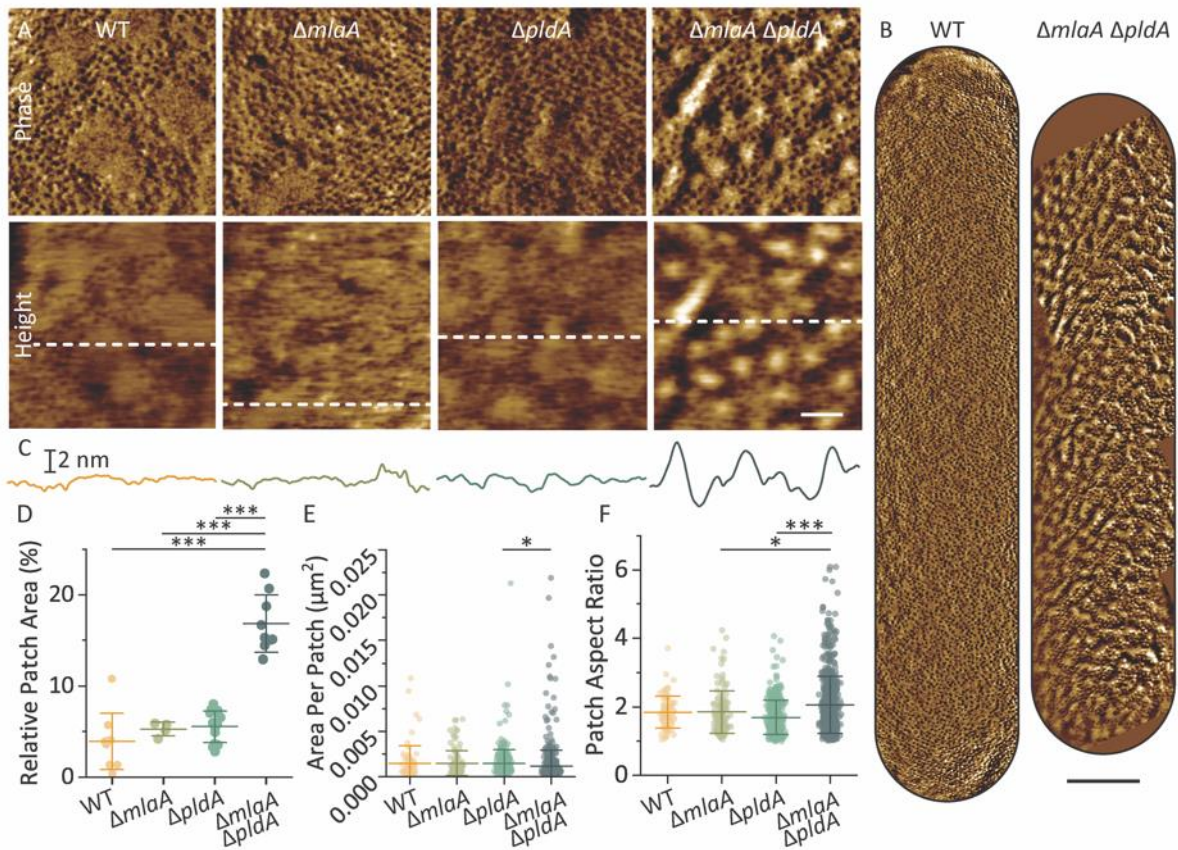
**Fig. 2. Within the trimeric porin network, distinct pore-free patches, that behave as liquid phases, can be seen.** (A) AFM phase image with patches highlighted by dashed lines. (B) Height image of the same area, showing that the patches protrude by about 1 nm. These regions are also extremely smooth, with height variations of less than 0.5 nm. (C) At time scales consistent with cell division, under these experimental conditions, patches merge, grow and split apart. (D) Schematic of OmpF labelling by colicin N<sup>1-185</sup>mCherry. Phase and height images of the same area are used to independently localise patches and labels, respectively. Quantification of the labels per area shows that OmpF co-localises with the pore network. (E) OmpA is labelled by expressing ompA with a streptavidin binding peptide in an outer loop and adding streptavidin. Quantification of the labels per area shows that OmpA also co-localises with pore networks. Each data point corresponds to a single image, where images were recorded from 3 independent experiments with at least 1 cell per experiment. Horizontal scale bars are (B and E) 100 nm and (C) 50 nm. Colour (phase/height) scales are (A) 1.5 deg, (B) 5 nm, (C) 1.5 deg, (D) 1.5 deg and 5 nm, (E) 0.3 deg and 5 nm. \*\* =  $p < 10^{-2}$  and \*\*\* =  $p < 10^{-4}$  from a paired two-way student's t-test.



1  
2 **Fig. 3. Patches are LPS-enriched domains.** (A) Western blot showing changes in LPS levels. (B) For low  
3 LPS levels (*lpxC101*), the cell area covered by patches is significantly smaller than for high LPS levels  
4 (*lpxC<sub>R230L</sub>*). Reintroduction of O-antigen and hence longer LPS (+*wbbL*) results in this area being almost  
5 twice that measured for WT (MG1655). Data were recorded in at least 3 independent experiments  
6 per condition; each data point represents 1 cell. (C) Longer LPS chains result in larger patches; and  
7 measurements for lower LPS expression suggest smaller patches. (D) Patch morphology (here  
8 quantified by the aspect ratio) does not noticeably vary with LPS expression. Each data point  
9 represents an individual patch from cells used in B. (E) Typical phase images used to quantify B-D.  
10 Horizontal scale bar is 50 nm. Colour (phase/height) scale is 1.5 deg. \* =  $p < 0.05$  and \*\* =  $p < 10^{-2}$ .

11





1

2 **Fig. 4. Outer-leaflet phospholipids lead to the formation of new domains.** (A) AFM phase and height  
 3 images of cells with mutations that disrupt lipid asymmetry in the OM. (B) Whole cell phase images of  
 4 a MG1655 and a  $\Delta pldA \Delta mlaA$  cell showing the extent of membrane reorganisation with abundant  
 5 phospholipids. (C) Height profiles of dashed lines in the AFM images in A. (D) For  $\Delta pldA \Delta mlaA$  cells, a  
 6 significantly larger fraction of the bacterial surface is covered by pore-free patches of either type,  
 7 compared with WT and single mutants. Data were recorded in at least 3 independent experiments per  
 8 condition; each data point represents 1 cell. (E) The mean area of each individual patch varies.  $\Delta pldA$   
 9  $\Delta mlaA$  cells also have a greater spread of patch sizes. Each data point represents an individual patch  
 10 from cells used in D. (F) The mean aspect ratios of  $\Delta pldA \Delta mlaA$  cells is higher than single mutants, an  
 11 example of an elongated patch can be seen in A. Horizontal scale bars are (A) 50 nm and (B) 200 nm.  
 12 Colour (phase/height) scales are (A) 0.75 deg and 5, 4, 5 and 5 nm. \* =  $p < 0.05$  and \*\*\* =  $p < 10^{-4}$ .

13